Magnetic Resonance in Medicine 46:324–334 (2001)

Imaging Longitudinal Cardiac Strain on Short-Axis Images Using Strain-Encoded MRI

Nael F. Osman,[1*] Smita Sampath,[2] Ergin Atalar,[1] and Jerry L. Prince[2]

This article presents a new method for measuring longitudinal strain in a short-axis section of the heart using harmonic phase magnetic resonance imaging (HARP-MRI). The heart is tagged using 1-1 SPAMM at end-diastole with tag surfaces parallel to a short-axis imaging plane. Two or more images are acquired such that the images have different phase encodings in a direction orthogonal to the image plane. A dense map of the longitudinal strain can be computed from these images using a simple, fast computation. Simulations are conducted to study the effect of noise and the choice of out-of-plane phase encoding values. Longitudinal strains acquired from a normal human male are shown. Magn Reson Med 46:324–334, 2001.

Key words: cardiac motion; harmonic phase; magnetic resonance tagging; myocardial strain

MRI is the only modality capable of directly imaging the motion inside the myocardium (1–6). MR tagging and phase contrast MRI are both capable of noninvasive and accurate measurements of myocardial motion. It is known that during systole the left ventricle (LV) of the heart deforms to reduce the volume of its cavity and ejects blood out of the ventricles. In a short-axis image of the LV, the wall muscle shows thickening in the radial direction and shortening in the circumferential direction. In a long-axis image of the LV, long-axis shortening is observed as the base moves toward the apex. These measures, oriented as they are in the natural coordinate system of the LV, are useful indices of myocardial health (7,14). Capturing this information from MR images requires the acquisition of long-axis images during MR tagging (5,6), or velocity encoding in the slice direction for phase contrast MRI (1). In this article we develop a technique to image longitudinal strain in short-axis images using a relatively new MR imaging concept, harmonic phase (HARP) MRI.

MR tagging uses special pulse sequences at end-diastole to create planes of saturated magnetization that are traditionally oriented orthogonal to the image plane (2–4). These tag surfaces bend with the deformation of the myocardium and their intersections with the image planes deform from straight lines into bent curves. To measure 3D motion, short-axis images are used to measure two motion components and long-axis images to measure the third (5,6). Detailed motion of the myocardium can be deduced by analyzing the deformation of the tag lines found within these images (7–10).

This overall imaging and analysis paradigm is problematic for the following reasons. First, fusing short-axis and long-axis data requires careful registration, which may be difficult or inaccurate because of patient movement over a long series of breath-holds. Second, because of time limitations the number of long-axis images that can typically be acquired is fairly small, say 8–10 images. This means that motion information in the long-axis direction is sparsely sampled in the axial images, only 16–20 rays emanating from the long axis. Finally, 3D motion computations typically require identification of both the tag lines and the LV geometry, which are typically difficult tasks requiring some manual intervention (11,12).

In this article, we describe a new method to measure longitudinal strain from short-axis images only. The imaging principle is based on MR tagging, but in sharp contrast to usual techniques we use tag planes that are initially oriented parallel to the image plane. The data processing principle is based on HARP-MRI, which analyzes the spectral peaks in *k*-space that are created by the tagging process (13–16). It turns out that by acquiring two images with two different *z* phase encodes, where the *z* direction is the slice select direction, a dense estimate of longitudinal strain on the short-axis image plane can be calculated. Each of the two acquired MR images depicts the underlying strain of the tissue as if the intensity is modulated by the local strain; thus, we call the method strain-encoded (SENC) imaging or SENC-MRI. In the following we describe the approach, show how it is implemented on an MR scanner, analyze trade-offs in performance as a function of image acquisition parameters, and give a result acquired from a normal human male.

LONGITUDINAL TAGGING AND STRAIN

Imaging Equation

Typically, MR tags are created so that their planar surfaces are orthogonal to the image plane. Here, however, we generate tag planes parallel to the image plane using the pulse sequence shown in Fig. 1. This 1-1 SPAMM pulse sequence uses two hard RF pulses, each giving a 90° tip angle. A magnetic field gradient $G(t)$ oriented in the slice-selection direction is placed between the two RF pulses and a crusher is placed at the end to spoil all transverse spins. This gradient $G(t)$ spatially modulates the longitudinal magnetization of the body in a sinusoidal pattern such that planes of constant sinusoidal phase are parallel to the image plane. The imaging parameters are selected so that the slice thickness is several times larger than the tag period.

[1]Department of Radiology, The Johns Hopkins University, Baltimore, Maryland.

[2]Center for Imaging Science, Department of Electrical and Computer Engineering, The Johns Hopkins University, Baltimore, Maryland.

Grant sponsor: National Heart, Lung, and Blood Institute; Grant number: R01HL4705.

*Correspondence to: Nael F. Osman, Department of Radiology, Johns Hopkins University, 601 N. Caroline St., Room 4243, Baltimore, MD 21287-0845. E-mail: nael@jhu.edu

Received 18 July 2000; revised 13 February 2001; accepted 16 February 2001.

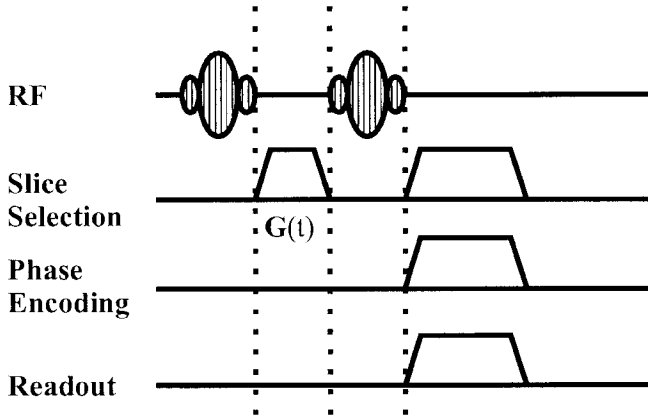

FIG. 1. A time diagram showing 1-1 SPAMM pulse sequence with a gradient in the *z*-direction.

To fully explain our method it is necessary to develop a mathematical model of the imaging process. Let the location of a point in the image plane be described by the vector $\mathbf{y} = [y_1\ y_2]^{\mathrm{T}}$ and let z describe the location orthogonal to the image plane. In this article, we consider short-axis images of the left ventricle (LV) of the heart, so the z-axis corresponds to the long-axis of the LV. To be specific, we let y_1 and y_2 correspond to the readout and phase-encode directions, respectively, and let $z = \mathrm{O}$ correspond to the image plane.

At time t_r, immediately after the tagging pulse sequence is played, the longitudinal magnetization can be written as (17) (assuming no relaxation during tagging):

$$M(\mathbf{y}, z, t_r) = \rho_H(\mathbf{y}, t_r)\cos(wz), \qquad [1]$$

where ρ_{H} is a function proportional to the proton density inside the voxel at $\mathbf{y}$. Here, we assume that the slice is thin enough that ρ_{H} does not depend on z inside a voxel. The cosine term arises from tagging; it has a spatial frequency given by $w = \gamma\int G(\tau)d\tau$ rad mm^{-1}, where γ is the gyromagnetic ratio for protons. The tag period is simply given by $2\pi/w$ mm^{-1}.

Tag Frequency

During systole the LV undergoes motion that causes myocardial displacement and deformation. The tag pattern moves with the tissue and generally undergoes both compression and tilting, as shown in Fig. 2a,b. It is clear that the tissue strain affects the frequency of the tag pattern. Our goal is to measure both the frequency and orientation of the tag pattern at $t > t_r$ within each voxel. This information is all that is needed to calculate a high-resolution map of longitudinal strain, in the Eulerian sense, of a short-axis slice.

As shown in Fig. 2c,d, we can represent the tag frequency inside a voxel with a vector whose direction is orthogonal to the tag planes and whose length is equal to the tag pattern's frequency. This local frequency vector can be decomposed into two components: $\nu(\mathbf{y},t)$, which is the component in the z-direction that depends primarily on the longitudinal strain; and $\boldsymbol{\omega}(\mathbf{y},t)$, which is the component in the imaging plane that depends primarily on the tissue tilt. The pattern inside a voxel, therefore, can be described as $\cos(\psi(\mathbf{y},z,t))$ whose phase ψ can be written as:

$$\psi(\mathbf{y}, z, t) = \phi(\mathbf{y}, t) + \nu(\mathbf{y}, t)z, \qquad [2]$$

where $\omega(\mathbf{y},t) = \nabla\phi(\mathbf{y},t)$—the spatial gradient of phase in the image plane.

Because of longitudinal relaxation, the tag pattern fades over the cardiac cycle. This phenomenon can be captured mathematically by simply adding another term (that does not involve the tag pattern) to the longitudinal magnetization, as follows:

$$M(\mathbf{y}, z, t) = \rho_0(\mathbf{y}, t) + \rho_H(\mathbf{y}, t)\cos(\psi(\mathbf{y}, z, t)). \qquad [3]$$

The term $\rho_0(\mathbf{y},t)$ is a function proportion to the proton density that grows in intensity over the cardiac cycle. Correspondingly, the term $\rho_H(\mathbf{y},t)$ decays with time.

Longitudinal Strain and Tilt Angle

Strain is defined as the change in length per unit length. Taking the tag period as a measure of length, we see that the reference length at pixel $\mathbf{y}$ is $2\pi/w$ and the deformed length is $2\pi/\sqrt{\omega(\mathbf{y}, t)^2 + \nu(\mathbf{y}, t)^2}$, where $\omega(\mathbf{y}, t) = \|\boldsymbol{\omega}(\mathbf{y}, t)\|$. After straightforward manipulation, we see that the strain is given by:

$$\epsilon(\mathbf{y}, t) = \frac{w}{\sqrt{\omega(\mathbf{y}, t)^2 + \nu(\mathbf{y}, t)^2}} - 1. \qquad [4]$$

Since the tags are originally oriented in the longitudinal direction, the strain computed in spatial coordinates is properly called the *Eulerian longitudinal strain*. It may be useful to measure the angle over which the tissue has tilted

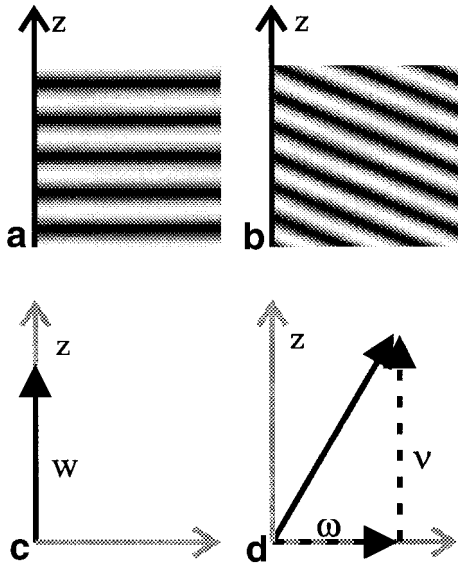

FIG. 2. The tag pattern inside a voxel at (**a**) t_r and (**b**) $t > t_r$. The local frequencies shown in **c** and **d** correspond to **a** and **b,** respectively.

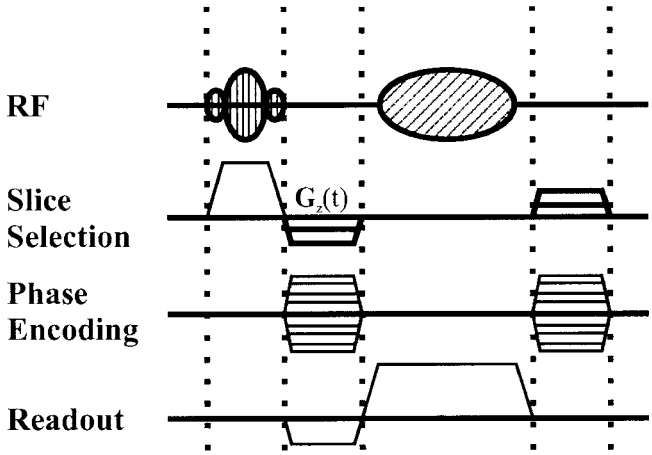

FIG. 3. A timing diagram showing a gradient echo pulse sequence with an additional gradient G_z.

from the longitudinal direction. We can calculate the *tilt angle* $\theta(\mathbf{y},t)$ of the tag pattern as follows:

$$\theta(\mathbf{y}, t) = \tan^{-1} \frac{\omega(\mathbf{y}, t)}{v(\mathbf{y}, t)}. \quad [5]$$

In order to measure the longitudinal strain and tilt angle, we must measure the tag local frequency components $\omega(\mathbf{y},t)$ and $v(\mathbf{y},t)$. The following section describes how to acquire and process MR short-axis images for this purpose.

MEASURING LOCAL FREQUENCY

Image Acquisition

In order to image the local frequencies of the voxels, a gradient field $G_z(\tau)$ in the z-direction is applied during the refocusing lobe of each TR, as shown in Fig. 3. This process can be seen as a phase encoding in the z-direction using the value $k_z = \gamma \int G_z(\tau)d\tau$. The resulting image is the integral, in the z-direction, of the longitudinal magnetization multiplied by the z-encode phase factor over the slice profile $f(z)$, or mathematically as:

$$I(\mathbf{y}, t; k_z) = \int_{-\infty}^{\infty} M(\mathbf{y}, z, t) f(z) e^{-jk_z z}\, dz. \quad [6]$$

The phase encode value k_z is made an explicit argument of I because we will be acquiring more than one image with different k_z's.

Using Eq. [3] and expanding the cosine function as a complex exponential, we can rewrite Eq. [6] as:

$$I(\mathbf{y}, t; k_z) = \rho_0(\mathbf{y}, t)F(k_z) + \rho_H(\mathbf{y}, t)e^{-j\phi(\mathbf{y},t)}F(k_z + v(\mathbf{y}, t)) + \rho_H(\mathbf{y}, t)e^{+j\phi(\mathbf{y},t)}F(k_z - v(\mathbf{y}, t)), \quad [7]$$

where $F(k)$ is the Fourier transform of the slice profile $f(z)$.

Equation [7] shows that the acquired image is a superposition of three images, each weighted by the Fourier transform of the slice profile evaluated at a specific frequency. If the tag frequency w is large enough and the strain and tilt small enough, then these images are well separated in their z-frequency content, as shown in Fig. 4. The bell-shaped profiles in this figure correspond to $F(\cdot)$ shifted to $-v$, 0, and $+v$ in k_z-space. The local frequency component v is dependent' on the strain and tilt, but is expected to be near w, the original tag frequency. The intensity of the acquired image at $\mathbf{y}$ depends on the slice profile, the strain, the underlying effective proton density, and other image acquisition parameters (e.g., TR, TE, etc.). Proper choice of parameters will yield peaks that are approximately nonoverlapping. If k_z is then selected to be close to $v(\mathbf{y},t)$, the resulting image is dominated by the peak centered at $v(\mathbf{y},t)$, yielding:

$$I(\mathbf{y}, t; k_z) \approx \rho_H(\mathbf{y}, t)e^{j\phi(\mathbf{y},t)}F(k_z - v(\mathbf{y}, t))). \quad [8]$$

Estimating v

The Fourier transform $F(k_z)$ of a typical slice profile $f(z)$ is real, symmetric, and centered at the origin ($k_z = 0$). Therefore, the location of a shifted version of this profile $F(k_z - v)$, where *location* is defined by either the peak or the center of mass, is v. Furthermore, from Eq. [8] we see that the location of $F(k_z - v)$ is also the location of $|I(\mathbf{y},t;k_z)|$ when k_z is near v.

Two ways to find v are immediately apparent: for each $(\mathbf{y},t)$ find either the peak or the center of mass of $|I(\mathbf{y},t;k_z)|$ with respect to k_z (in the vicinity of v). Acquiring a large number of k_z samples for this purpose is impractical; however, it is possible to estimate both the peak and the center of mass from a smaller number of samples. Estimating the peak requires specific knowledge of the slice profile, is sensitive to noise, and is computationally intensive. Instead, we have developed an approach based on the computation of the center of mass, which requires only two k_z image samples, uses a fast computation, and applies a simple correction factor to account for the specific slice profile.

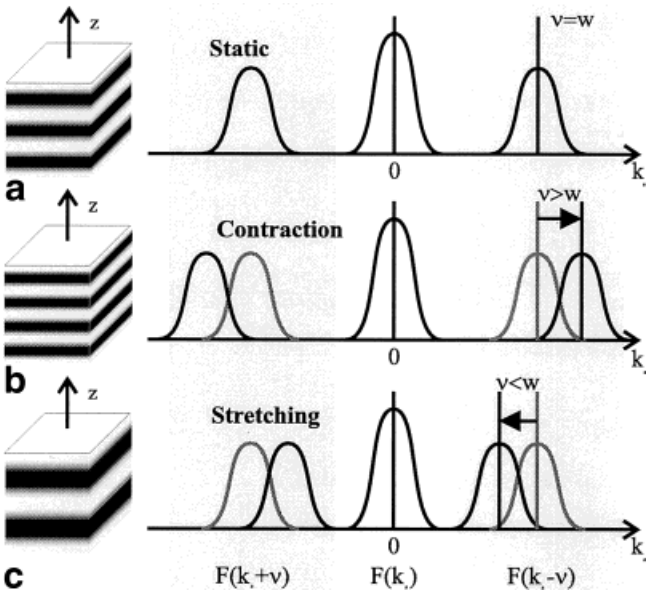

FIG. 4. Frequency content in the z-direction for a voxel having no strain, being compressed, or being stretched.

The center of mass of $F(k_z - \nu)$ can be estimated from $I(\mathbf{y},t;k_z)$ using the following discrete approximation:

$$\hat{\nu}(\mathbf{y}, t) = \frac{\sum_{k_z} k_z |I(\mathbf{y}, t; k_z)|}{\sum_{k_z} |I(\mathbf{y}, t; k_z)|}, \quad [9]$$

where it is assumed that the k_z samples are selected in the vicinity of ν. Again, it is impractical to acquire the large number of k_z samples necessary to make this approximation accurate; instead, we consider what can be accomplished with only two images: $I_a(\mathbf{y},t) = I(\mathbf{y},t;w_a)$ and $I_b(\mathbf{y},t) = I(\mathbf{y},t;w_b)$. In this case, the discrete approximation to the center of mass is given by:

$$\mu(\mathbf{y}, t) = \frac{w_a |I_a(\mathbf{y}, t; w_a)| + w_b |I_b(\mathbf{y}, t; w_b)|}{|I_a(\mathbf{y}, t; w_a)| + |I_b(\mathbf{y}, t; w_b)|}. \quad [10]$$

In general, μ is not always a good approximation to ν; however, a simple correction that depends on the slice profile can be made to yield an accurate estimator. Before describing this, we consider how to choose the two z phase encode values w_a and w_b.

In order to isolate the spectral component of $I(\mathbf{y},t;k_z)$ dependent on ν, both w_a and w_b must be chosen to be near ν. We know that $\nu = w$ (the tag frequency) in the absence of strain, that $\nu > w$ when there is tissue compression, and that $\nu < w$ when there is tissue stretching or tilting. In a normal heart, we expect the range of possible local frequencies to be limited to a range $[\nu_{\min}, \nu_{\max}]$, which depends on both the normal longitudinal strain and the tag frequency. (Tilting can be factored in here if necessary but is usually small enough to be neglected in this approximation.) It is reasonable to select the phase encode values to be $w_a = \nu_{\min}$ and $w_b = \nu_{\max}$, as shown in Fig. 5.

The quantity $\mu(\mathbf{y},t)$ can be calculated quickly from two images and it is approximately equal to $\nu(\mathbf{y},t)$; however, it is not exactly equal to $\nu(\mathbf{y},t)$ in general. Consider the situations depicted in Fig. 5. If $\nu_{\min}$ and $\nu_{\max}$ are equidistant from w and there is no strain, as shown in Fig. 5a, then $\mu = \nu$. If $\nu = \nu_{\min}$ or $\nu = \nu_{\max}$, as shown in 5b and 5c, then $\mu = \nu$ also. However, in other situations, such as depicted in panel 5d, $\mu \neq \nu$, in general. An interesting case in which $\mu = \nu$ for any value of ν is that in which the slice profile is a perfect rectangle (18,19). This is not practically possible to generate, so it is only of academic interest. It is possible, however, to produce a profile whose Fourier transform is of a finite number of sinc lobes, which would have a perfect relation in some range.

Although it is very informative to view the image $\mu(\mathbf{y},t)$ (see the Results section), it is also important to generate an accurate estimate of ν so that the strain can be determined. We accomplish this using a simple correction to $\mu(\mathbf{y},t)$. An approximate relationship between $\mu,(\mathbf{y},t)$ and $\nu(\mathbf{y},t)$ can be found by substituting Eq. [8] into Eq. [10], which yields (after simplification):

$$\mu(\mathbf{y}, t) = \mathrm{Re}\left\{\frac{w_a F(w_a - \nu(\mathbf{y}, t)) + w_b F(w_b - \nu(\mathbf{y}, t))}{F(w_a - \nu(\mathbf{y}, t)) + F(w_b - \nu(\mathbf{y}, t))}\right\}. \quad [11]$$

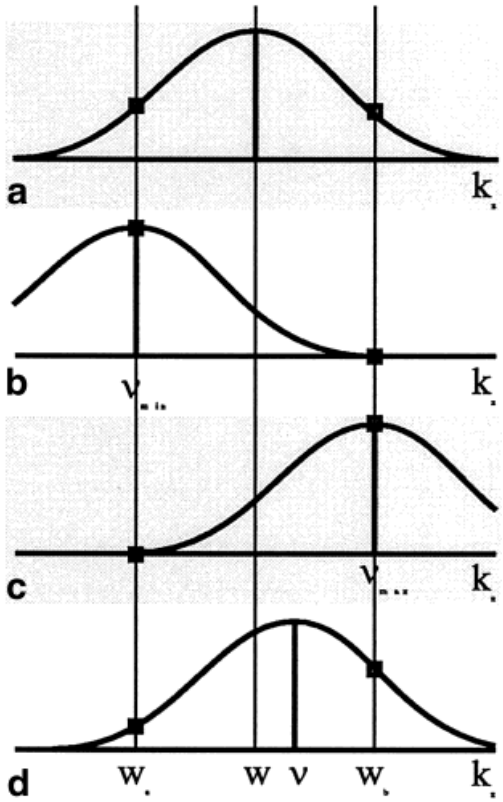

FIG. 5. Measuring ν from two samples at w_a and w_b. (**a**) $\nu = w$, (**b**) $\nu_{\max}$, (**c**) $\nu_{\min}$, and (**d**) arbitrary ν.

This relationship can be summarized by the expression:

$$\mu(\mathbf{y}, t) = \beta(\nu(\mathbf{y}, t)), \quad [12]$$

in which the function $\beta(\cdot)$ depends on the Fourier transform $F(k_z)$ of the slice profile and on w_a and w_b. We will show empirically in the Results section that $\beta(\cdot)$ is monotonic between w_a and w_b—so that it can be inverted, and that it is even well-approximated by a linear relationship in this range, which is trivial to invert. Therefore, after calculating $\mu(\mathbf{y},t)$ we apply the transformation:

$$\hat{\nu}(\mathbf{y}, t) = a\mu(\mathbf{y}, t) + b, \quad [13]$$

to estimate $\nu(\mathbf{y},t)$ for suitable choices of the constants a and b, which are determined a priori.

Estimating ω

The local frequency $\boldsymbol{\omega}(\mathbf{y},t)$ is the spatial gradient of $\phi(\mathbf{y},t)$. Since $F(k_z)$ is real, it follows from Eq. [8] that $\phi(\mathbf{y},t)$ is just the phase of an acquired image $I(\mathbf{y},t;k_z)$, irrespective of k_z. Computing ϕ itself is problematic because of phase wrapping—i.e., the computed value ends up wrapped to the range $[-\pi, +\pi]$. However, the spatial gradient of phase can be readily computed and is in fact the basis of the standard harmonic phase MRI technique (13,15,16).

Two images are acquired in order to compute ν, and hence we have both available to compute ω. The two images have the same phase. Figure 5 shows that one

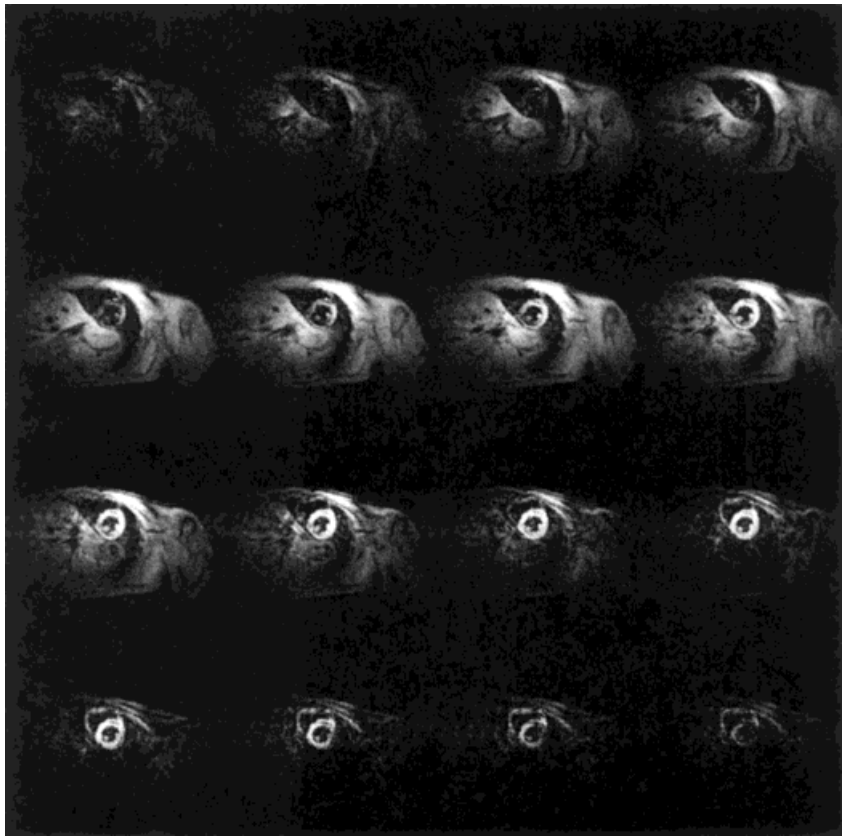

FIG. 6. Short axis images of the heart obtained for different values of *z*-direction phase encode with a 2.5 mm tag period out-of-plane, sinusoidal tag pattern. Going across the rows from top-left to bottom-right, the *z* phase encode values are 0.35 to 0.50 mm^{-1} in increments of 0.01 mm^{-1}.

image may have a higher intensity than the other or they may be comparable in intensity. Since low-intensity images are prone to noise, and thus give less accurate phase computation, we chose to compute the phase using the sum of these images.

In summary, ω is given by:

$$\omega(\mathbf{y}, t) = \nabla \tan^{-1} \frac{\mathrm{Im}\{I(\mathbf{y}, t; w_a) + I(\mathbf{y}, t; w_b)\}}{\mathrm{Re}\{I(\mathbf{y}, t; w_a) + I(\mathbf{y}, t; w_b)\}}. \quad [14]$$

The numerical implementation of the spatial gradient ∇ must be done carefully to avoid problems with the wrapping artifact (see Ref. 16). The magnitude $\omega(\mathbf{y},t) = |\boldsymbol{\omega}(\mathbf{y},t)|$ is used in the computation of the tilt angle $\theta(\mathbf{y},t)$ using Eq. [5].

EXPERIMENTS

Normal Human Heart

Experiments were performed on a 1.5 T GE Signa whole-body MR scanner (Signa, General Electric Medical Systems, Milwaukee, WI). A segmented *k*-space gradient-echo pulse sequence modified from that reported in Ref. 20 was used. The modifications included the abilities to generate tags oriented in the *z*-direction and to acquire *z*-direction phase encodes.

Images of a normal male volunteer, age 30, were acquired with the approval of the Joint Committee on Clinical Investigation and after obtaining written approval and consent. The subject was fitted with a phased array coil and instructed to hold his breath at end-exhalation. Out-of-plane tags with a tag period of 2.5 mm were applied just after the QRS trigger. The following scanner settings were used for image acquisition: slice thickness = 15 mm, FOV = 48 cm, TR = 6.8 ms, and TE = 1.8 ms. Image acquisition was delayed 300 ms from end-diastole and successive *y* phase-encodings were acquired. In subsequent heartbeats additional *y* phase-encodings were acquired so that an entire image was imaged in a single breath-hold. Overall, 128 phase-encodings were acquired, each had 256 samples.

Over the course of the experiment 17 images were acquired with *z* phase encode values of 0.35, 0.36,…,0.51mm^{-1}. Using segmented *k*-space with eight views per segment, each image was acquired with a 16-sec breath-hold. The first 16 of these images are shown in Fig. 6. It is helpful to refer to Fig. 4 to understand these images. There are two dominant tissue types in this cross-section: static tissue whose tag frequency has not changed, and cardiac muscle whose tag frequency has increased. Therefore, there are two *z*-spectra that are being sampled with the different *z*-encodes, as depicted graphically in Fig. 4b (positive frequency axis). The top row of Fig. 6 shows very little signal at first and then shows increasing intensity in the static tissues; the signal from the cardiac tissue is small. The second row shows a fairly constant intensity in the static tissues, while the cardiac tissue is gaining in brightness. In the third row the static tissue is fading while the cardiac tissue intensity remains fairly constant, and in the fourth row both signals fade out.

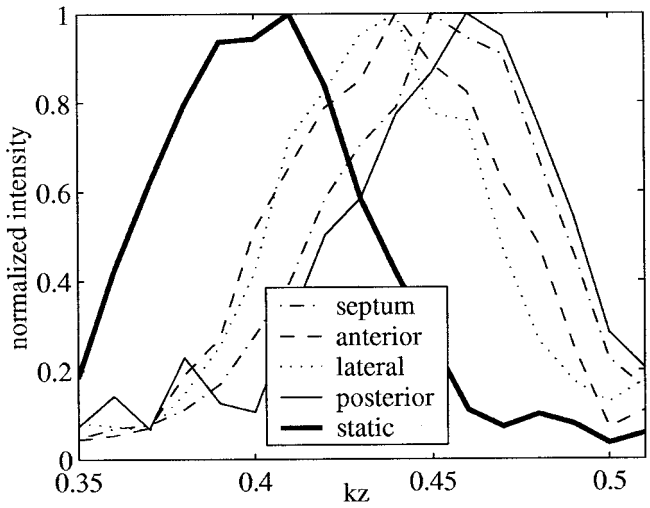

FIG. 7. Plots showing the average intensity at different regions in the image with respect to k_z. The curves are normalized.

Although there are two dominant tissue types in Fig. 6, there are more subtle variations in the intensity variations within each tissue class. To demonstrate these variations in the myocardium, we manually selected four regions of interest (ROIs), each 3 × 3 matrix of pixels, near the midwall in the septal, anterior, lateral, and posterior regions of the heart. The average image intensity within each ROI is plotted as a function of k_z in Fig. 7. For reference, a k_z-profile from an ROI containing static tissue is plotted as well, and for clarity all curves were normalized to have the same peak intensity. As illustrated in the figure, the curves representing the different regions of the heart are shifted to higher frequencies relative to the static tissue. The extent of the shift differs for the different regions. The highest shift centered around 0.46 mm^{-1} represents the highest contraction of 13% in the longitudinal direction.

A center of mass calculation applied pixel-by-pixel to the 17 acquired images yields the image shown in Fig. 8a. This image comprises an estimate of the local frequency ν, the z-axis component of the local frequency vector. The magnitude of the in-plane component is ω, which is shown in Fig. 8b. This image is computed using:

$$\omega(\mathbf{y}, t) = \left\| \nabla \tan^{-1} \frac{\mathrm{Im}\left\{ \sum_{k_z} I(\mathbf{y}, t; k_z) \right\}}{\mathrm{Re}\left\{ \sum_{k_z} I(\mathbf{y}, t; k_z) \right\}} \right\|, \qquad [15]$$

which extends Eq. [14] to the case of more than two acquired images. In order to apply Eq. [15], it was necessary to remove a linear phase roll that occurs in the z-direction. It is not necessary to do this when there are only two images, for reasons explained below. Given the images of ν and ω, it is straightforward to compute the tilt angle using Eq. [5] and the Eulerian longitudinal strain using Eq. [4]. These images are shown in Fig. 8c,d, respectively.

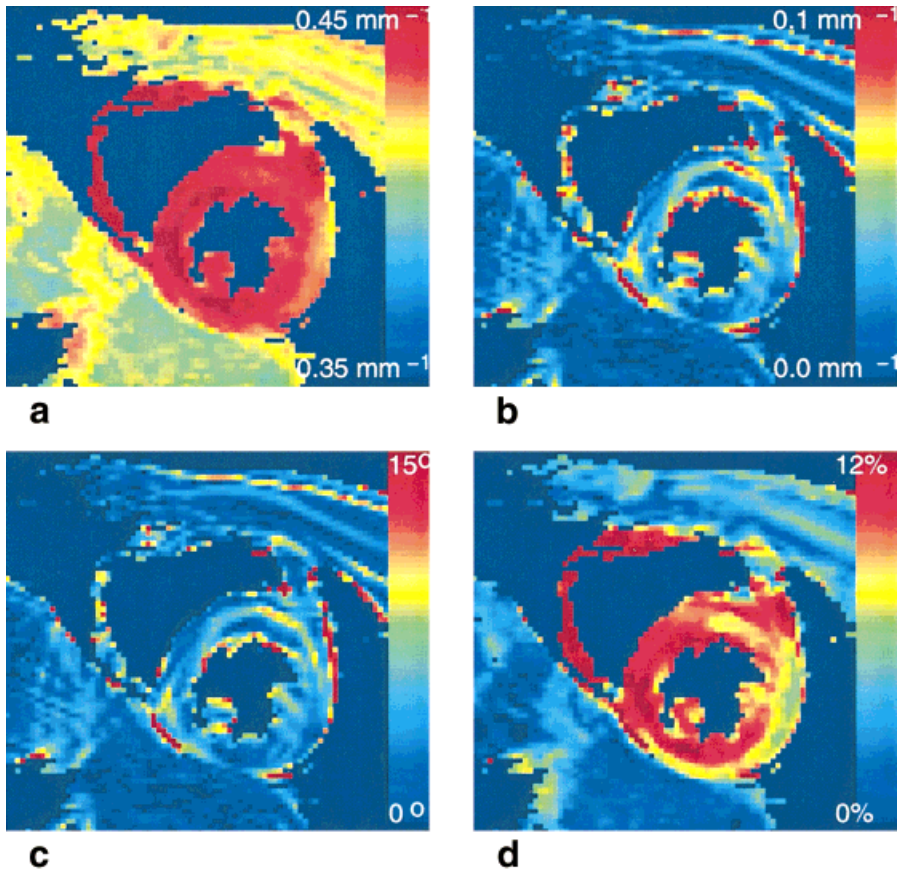

FIG. 8. (**a**) The local frequency ν, (**b**) the local frequency ω, (**c**) the tilt angle, and (**d**) the Eulerian longitudinal strain, all calculated from 17 acquired images.

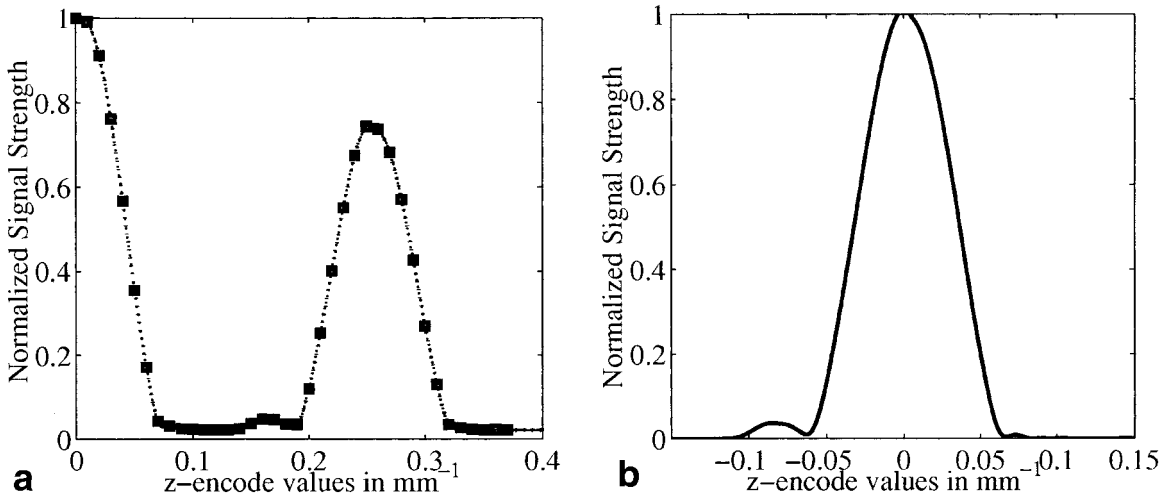

FIG. 9. **a:** Average phantom signal strength as a function of k_z. **b:** Estimate of the Fourier transform of the slice profile.

Several observations can be made from Fig. 8. Figure 8a reflects the overall frequency shift observed in the ROI plots in Fig. 7. Here, the myocardium is quite distinguished from the static tissue owing to its longitudinal compression alone. Figure 8b,c are very similar, which is to be expected, since the tilt angles are very small—less than 15°. These images reveal a somewhat diffuse or random pattern of tilt, not overtly structured within the myocardium. Figure 8d, which shows the Eulerian longitudinal strain, is the goal that is sought after. It shows that the strain is pronounced in the myocardium, distinguished almost to the point that a simple threshold would segment the myocardium. It should be noted that the right ventricular myocardium shows pronounced longitudinal strain in this technique despite it being quite thin relative to the pixel size of the image. Overall, in this normal heart the Eulerian longitudinal strain falls in the range of 6–12% within the myocardium.

It is impractical to acquire many images in order to compute longitudinal strain. To implement the approach using only two images, as outlined above, it is necessary to determine the slice profile, to optimize the selection of w_a and w_b, and to determine β and its linear approximation. The following sections present these steps in detail.

Slice Profile

It is possible to determine the slice profile analytically given knowledge of the gradient and RF waveforms used in the pulse sequence. We chose to confirm our understanding of this process with a simple phantom experiment. A cylindrical glass vessel filled with water was used as the phantom. An external ECG trigger was used to emulate a heart rate of 60 bpm. The tagging pulse was applied just after the QRS trigger. The scan parameters were a tag separation of 4 mm, a slice thickness of 14 mm, a FOV of 48 cm, a TR of 4.264 ms, and a TE of 1.273 ms. Thirty-nine images were acquired for z phase encode values ranging from 0.0–0.37 mm^{-1}.

A fixed ROI was selected within the phantom and the average intensity was computed for each of the 39 images. The squares in Fig. 9a depict these computed intensities as a function of k_z. The dotted line in this figure represents a cubic spline fit to these data points. The Fourier transform $F(k_z)$ of the slice profile was obtained by extracting that portion of the curve corresponding to the spectral peak of the tagged image and shifting it to the frequency origin. This result is shown in Fig. 9b. Note the extra lobe caused by the shape of the RF pulse. This lobe will not affect our computations, as we will show.

We note also that the data acquired for the normal human used a slice thickness of 15 mm rather than 14 mm, as in this phantom experiment. We used simple space or frequency scaling to adjust this slice profile to that used in the human study.

Determining β

In order to accurately calculate strain and tilt angle from just two acquired images, it is necessary to determine the function β, as defined in Eqs. [11] and [13]. This function depends on both the slice profile and the two z phase encode frequencies w_a and w_b. In this section, we first describe how to select w_a and w_b and then describe the linear approximation of β.

It is clear from Eq. [11] that μ is a convex combination of w_a and w_b; hence, $w_a \leq \mu \leq w_b$. To maximize the dynamic range of μ, we would like to choose the difference $w_b - w_a$ to be as large as possible. But examination of Fig. 9b reveals a limitation. It would not be appropriate to pick $w_b - w_a$ to be any larger than the separation between the peak of this frequency profile and its first zero, as that would allow certain changes in v to have no effect on the calculated μ. Since the frequency profile in Fig. 9b is approximately the main lobe of a sinc pulse, one-half of the width of the main lobe is equal to the inverse of the slice thickness. Therefore, we chose the separation between w_a and w_b to be equal to or slightly less than the inverse of the slice thickness. For the human study described above, we set $w_b - w_a = 0.06$ mm^{-1}, which is slightly less than 1/15 mm^{-1}.

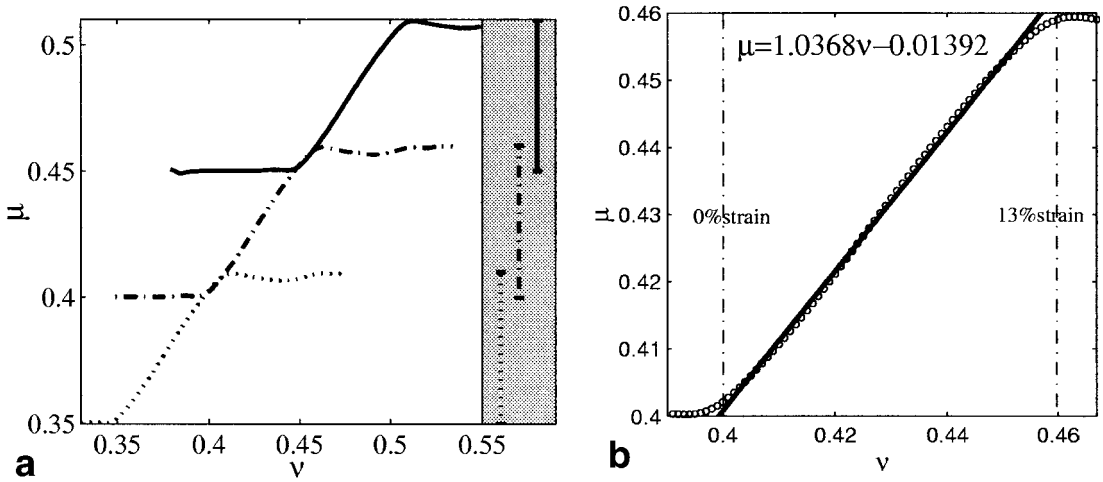

FIG. 10. **a:** The relation between ν and μ are shown for three combinations of w_a and w_b, maintaining a constant separation of 0.06 mm^{-1} between them. **b:** The case of $w_a = 0.40$ and $w_b = 0.46$, and the line approximation of the linear part of the curve.

We now consider three pairs of w_a and w_b values: $w_a = 0.35\ mm^{-1}$ and $w_b = 0.41\ mm^{-1}$, $w_a = 0.40\ mm^{-1}$ and $w_b = 0.46\ mm^{-1}$, and $w_a = 0.45\ mm^{-1}$ and $w_b = 0.51\ mm^{-1}$. For each pair we used Eq. [11] to compute μ, for a collection of ν's ranging from $0.33–0.55\ mm^{-1}$. The three plots are shown in Fig. 10a. For reference, the range of possible μ,'s that could be computed from each pair are indicated on the graph on the right side of this plot. The three cases depicted in Fig. 10a are similar in shape, but are shifted relative to one another. These three plots, in fact, sample a family of β functions having a similar shape that span a range of coverage in μ and ν.

In practice, β is used to calculate ν given μ. From Fig. 10a we see that w_a (and $w_b = w_a + 0.06\ mm^{-1}$) should be selected according to the expected range of actual ν values resulting from longitudinal tissue strain. For example, from the figure we see that if $w_a = 0.35\ mm^{-1}$ we can measure $\nu \in [0.35,0.41]\ mm^{-1}$ and if $w_a = 0.45\ mm^{-1}$ we can measure $\nu \in [0.45,0.51]\ mm^{-1}$. For the normal heart study, we observed that ν ranged from $0.40–0.46\ mm^{-1}$, which corresponds to strains in the range 0–13% contraction. This range of local frequencies is covered by the case $w_a = 0.40\ mm^{-1}$ and $w_b = 0.46\ mm^{-1}$.

Although β can be inverted using a look-up table, a spline approximation, or a fixed point algorithm, it is quite accurate and computationally faster to approximate it by a linear function. Although β saturates for certain regions of ν, it can be observed from Fig. 10a that it is approximately linear over the range of feasibly computed μ's. Thus, the large errors in the saturation regions have no practical consequence. For the case of $w_a = 0.40\ mm^{-1}$ and $w_b = 0.46\ mm^{-1}$, we found that β is well approximated in the central region by the linear relationship:

$$\mu = 1.0368\nu - 0.01392. \qquad [16]$$

A plot of this β function and its linear approximation is shown in Fig. 10b.

Strain From Two Images

From the 17 images acquired in the above human study, we selected the two images corresponding to $w_a = 0.40\ mm^{-1}$ and $w_b = 0.46\ mm^{-1}$, as shown in Fig. 11. Notice that the heart is less prominent in Fig. 11a than 11b, this is because the heart has higher frequency than the surrounding tissue. Notice also that the lateral epicardium is brighter in 11a than other parts of the heart, indicating lower longitudinal strain.

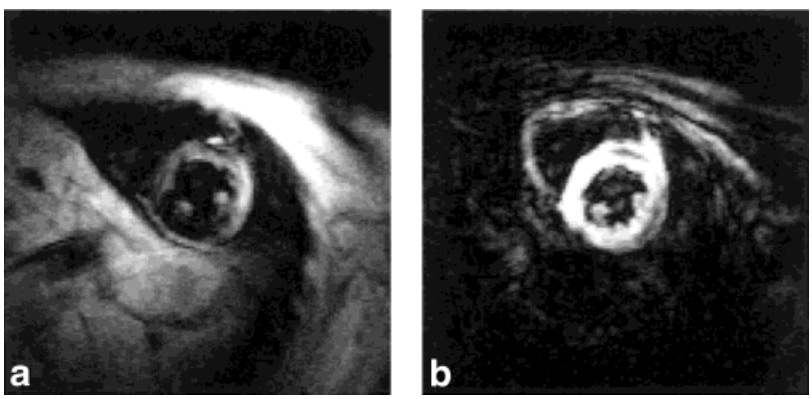

FIG. 11. The two images corresponding to (**a**) $w_a = 0.40$ and (**b**) $w_b = 0.46\ (mm^{-1})$.

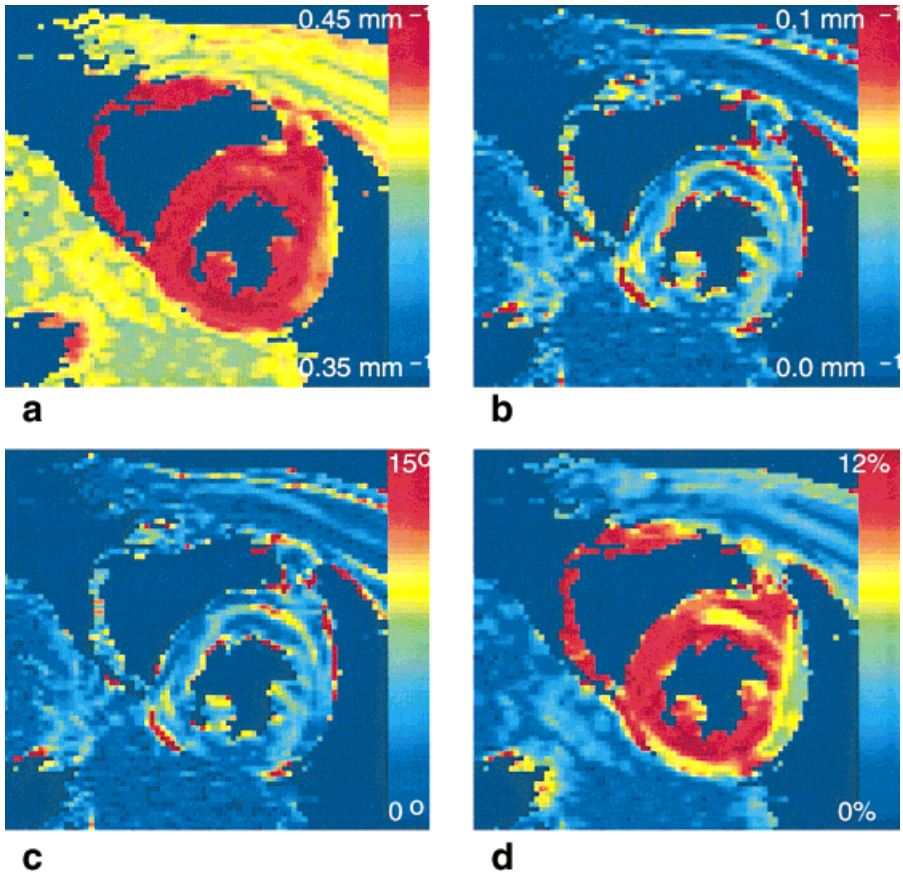

FIG. 12. (**a**) The local frequency ν, (**b**) the local frequency ω, (**c**) the tilt angle, and (**d**) the Eulerian longitudinal strain, all calculated from two acquired images.

We calculated $\mu(\mathbf{y},t)$ using Eq. [10] and inverted Eq. [16] to yield the following local frequency estimate:

$$\hat{\nu}(\mathbf{y}, t) = 0.9645\mu(\mathbf{y}, t) + 0.0134, \qquad [17]$$

which is shown in Fig. 12a. This image (and all images in Fig. 12) should be compared to the corresponding image in Fig. 8, which was computed using all 17 images.

The in-plane local frequency $\omega(\mathbf{y},t)$, shown in Fig. 12b, was computed by taking the complex modulus of $\omega(\mathbf{y},t)$, which was in turn computed using Eq. [14]. In contrast to the case when all 17 images were used to compute ω, there is no problem with z-phase roll when only two images are used. This is because the separation of k_z encodes provided by w_a and w_b tends to produce one image with small intensity, so the acquired phases do not add destructively. This is an unexpected advantage of working with only two acquired images.

The tilt angle $\theta(\mathbf{y},t)$ and Eulerian longitudinal strain $\epsilon(\mathbf{y},t)$ were computed from $\nu(\mathbf{y},t)$ and $\omega(\mathbf{y},t)$ using Eqs. [5] and [4]. These images are shown in Fig. 12c,d, respectively. Comparison of the images in Fig. 12 with those in Fig. 8 reveals very little difference. In fact, the root-mean-square (rms) difference between the two strain images is only around 1%, a very small difference.

Sensitivity to Noise

In order to measure the sensitivity of this method to noise, simulations to estimate the error in measuring the local frequency ν were done. Based on the slice profile, and for a certain value of ν, we computed image intensities:

$$I_a = F(w_a - \nu) + n_r + jn_i \quad \text{and} \quad I_b = F(w_b - \nu) + n_r + jn_i, \qquad [18]$$

where n_r and n_i are two normal random variables with a standard deviation σ. Using Eq. [10] $\hat{\mu}$ was calculated, from which followed the computation of $\hat{\nu}$ using Eq. [16].

The error $\tilde{\nu}$ in estimating ν in percent was calculated as:

$$\tilde{\nu} = \frac{\nu - \hat{\nu}}{\nu} \times 100,$$

and the error in estimating the strain in percent was:

$$\tilde{\epsilon} = \left(\frac{w}{\nu} - \frac{w}{\hat{\nu}}\right) \times 100.$$

These computations were repeated a large number of times and the rms value of the two errors was obtained for different values of σ between 0 and 20% of the peak value of F with ν varying between 0.4 and 0.46 mm^{-1}. The results are shown in Fig. 13.

Figure 13 shows that the estimated errors monotonically increase with the noise level σ. It is obvious, however, that the errors are not very large. In the case of our normal human heart study, we measured the maximum noise

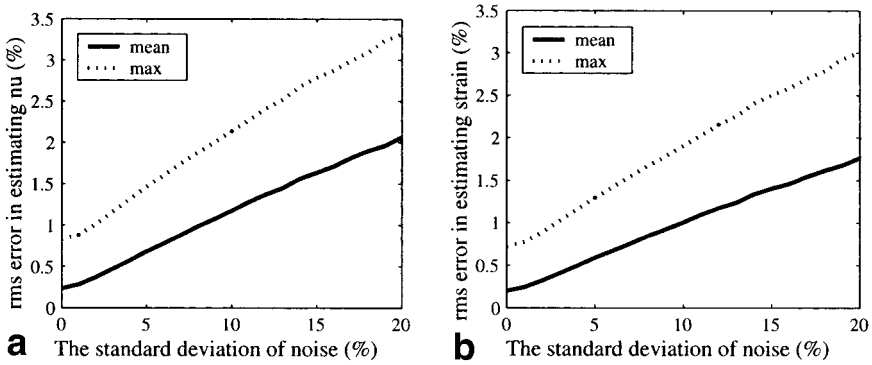

FIG. 13. **a:** The rms error in estimating ν (as a percentage of the actual value) with respect to noise σ. **b:** The corresponding error in estimating the strain.

level for all the points inside the LV. We found that σ does not exceed 4% of the peak intensity of a pixel. Therefore, we conclude that the error in measuring the strain should not exceed 1.5%.

DISCUSSION

There are many proposed methods for measuring the in-plane components of myocardial strain using MR tagging (15,21,22). All require acquisition of short-axis images, sometimes a single image with grid tags and sometimes a pair of one-dimensionally tagged images. There are also many proposed methods for calculating three-dimensional motion and strain using MR tagging (10,21,23). All of these approaches require long-axis images. Based on phase contrast techniques, Robson and Constable (24) were successfully able to measure the complete strain rate in a short-axis slice; however, their method was based on using a specific rectangular slice profile. Also, integration operations are required in order to obtain the actual longitudinal strain during systole. The proposed method, however, is based on tagging and is capable, therefore, of measuring the actual longitudinal strain without integration.

It is important to recognize potential limitations in our approach. First, this approach can be combined with standard 2D HARP methods to investigate both in-plane and longitudinal strain, but this will not produce a full 3D strain tensor. This is because the out-of-plane shear components cannot be measured using a tag vector pointing orthogonal to the plane. This can potentially be solved by using tag vectors that have both in-plane and longitudinal components (see Ref. 25, for example).

Another potential limitation is in the requirement that the range of strains and tilt angles be known a priori. It is observed from the plots of β in Fig. 10a that true local frequencies ν outside the approximately linear range of β saturate to either w_a or w_b. This may be acceptable behavior, particularly if myocardium yielding ν above w_b are considered normal and myocardium yielding ν below w_a are considered abnormal. In this case, the actual strain calculations will be inaccurate outside the linear range, but the results can still be used for diagnosis. Furthermore, in these cases another image or set of images could be acquired to resolve the saturation problem.

Another way to address local frequency saturation is to change the slice thickness. In particular, if a larger range between w_a and w_b is required the width of the Fourier transform of the slice profile should be increased. This means that the physical image slice should be thinner. While this is practically possible, it is important to be aware of several limitations. First, the SNR of the images decrease as the slice thickness decreases; therefore, the accuracy of the result will degrade. It is important to note that it is not necessary that the same tissue be present in the slice at the imaging time as the tag time. This is an Eulerian strain that is measured, so the strain of whatever tissue is in the slice at image time is measured. Second, a wider Fourier transform may cause spectral overlap with the DC spectrum (see Fig. 4). This is easily corrected by using a higher tag frequency which pushes the harmonic peak to a higher frequency. A potential benefit in the use of a thinner slice is that the approximation of a constant strain within the slice is better, but the effect of increased noise may well negate this benefit.

It is a useful exercise to explore what slice thickness, tag frequency, and *z*-encode values would be required to image the full range of expected longitudinal strain in the human normal heart. Let us assume that there is 0–20% longitudinal strain in a normal heart and that a zero tilt angle is possible. From Fig. 5 we see that $w_a = w$ and $w_b = 1.25w$ are the desired settings. Let us assume that the slice profile is approximately rectangular, so that its Fourier transform is approximately a sinc function. It follows that the frequency separation between the Fourier peak and its first zero is $1/d$, where d is the slice thickness; thus, $w_b - w_a = 1/d$ and:

$$0.25w = \frac{1}{d}. \qquad [19]$$

To prevent spectral overlap it is necessary that $w \geq 1/d$, which is automatically satisfied by Eq. [19].

It is convenient to rewrite Eq. [19] using the tag period $T = 1/w$, yielding:

$$d = 4T, \qquad [20]$$

which requires there be four tag periods within the imaged slice. Examination of the parameters used in our human study reveals $d = 6T$. There are two ways to understand this choice of parameters. First, it might be thought that a slightly thicker than optimal slice thickness was used to improve signal-to-noise. Second, by inverting the above

steps one sees that this choice is optimal if one assumes a maximum strain of 16%. (In this particular study the maximum strain was only about 13%.) The key trade-off is revealed here: one can increase SNR by increasing slice thickness, but this is at the expense of being able to measure larger strains.

The results presented here were for a single normal volunteer. In abnormal heart motion, we might expect lower strains, larger tilt angles, and stretching. The first two phenomena reduce the range of expected longitudinal frequencies, while the last phenomenon produces longitudinal frequencies below the tag frequency. After further study it may be possible to design pulse sequences for expected cardiac conditions or to simply adapt the image acquisition parameters "on the fly." The design principles are analogous to those introduced in the analysis of normal motion given above.

A very interesting observation can be seen in the heart images produced by this method. We can see that the blood signal is low, as if a blood-suppression technique has been used—which is not true. This can be explained in light of the motion of the blood. Like tissue, blood is tagged by the 1-1 SPAMM pulse sequence. However, because of the motion of the blood the tag pattern inside the blood is completely spoiled by the imaging time, and no signal from the blood could be observed at the harmonic peaks. More than that, because we are using a high-frequency tag pattern (equivalent to 2.5 mm tag separation), a motion within 20 ms period after tagging is sufficient to spoil the blood's tag pattern in a normal heart.

It is worth mentioning that the FOV used in our experiments, in this study, was relatively large (48 cm). This was done in order to improve the SNR of the resulting images, because of the fading of the harmonic peaks due to the tags fading. We are currently working on improving the SNR by tuning the imaging prescription.

CONCLUSION

We propose a new method, called SENC-MRI, for measuring the strain orthogonal to the imaging plane. The method requires the acquisition of two images with two phase encodings orthogonal to the image plane. Computation of longitudinal strain from these images is straightforward and fast. Preliminary results are encouraging; however, further validation is required.

In the future, SENC-MRI can be combined with standard HARP methods, which we have developed in previous research. This would allow one to acquire maps of the 3D primary (nonshear) strain components in short-axis images. Multiple short-axis images could be acquired to produce 3D volume distributions of strain, without the need for long-axis images. Further studies need to be conducted to determine optimal parameters for both 2D and 3D studies.

ACKNOWLEDGMENTS

We thank Drs. David Bluemke, Joao Lima, Jerome Carot, and Bernhard Cerber for their valuable help.

REFERENCES

1. Pelc NJ, Herfkens RJ, Shimakawa A, Enzmann D. Phase contrast cine magnetic resonance imaging. Magn Reson Q 1991;7:229–254.
2. Zerhouni EA, Parish DM, Rogers WJ, Yang A, Shapiro EP. Human heart: tagging with MR imaging—a method for noninvasive assessment of myocardial motion. Radiology 1988;169:59–63.
3. Axel L, Dougherty L. MR imaging of motion with spatial modulation of magnetization. Radiology 1989;171:841–845.
4. Axel L, Dougherty L. Heart wall motion: improved method of spatial modulation of magnetization for MR imaging. Radiology 1989;172:349.
5. McVeigh ER. Regional myocardial function. Cardiol Clin 1998;16:189–206.
6. Denney TS Jr, Prince JL. Reconstruction of 3D left ventricular motion from planar tagged cardiac MR images: an estimation theoretic approach. IEEE Trans Med Imag 1995;14:625–635.
7. McVeigh ER, Zerhouni EA. Noninvasive measurement of transmural gradients in myocardial strain with MR imaging. Radiology 1991;180:677–683.
8. Denney TS Jr, Prince JL. 3D displacement field reconstruction on an irregular domain from planar tagged cardiac MR images. In: Proc IEEE Workshop on Non-rigid and Articulate Motion, Austin, TX; 1994.
9. Denney TS. Identification of myocardial tags in tagged MR images without prior knowledge of myocardial contours. In: Duncan J. Gindi G, editors. Proc Information Processing in Medical Imaging, Lecture Notes in Computer Science, Poultney, VT; June 1997. New York: Springer-Verlag. p 327–340.
10. Denney TS Jr, McVeigh ER. Model-free reconstruction of three-dimensional myocardial strain from planar tagged MR images. J Magn Reson Imag 1997;7:799–810.
11. Guttman MA, Prince JL, McVeigh ER. Tag and contour detection in tagged MR images of the left ventricle. IEEE Trans Med Imag 1994;13:74–88.
12. Kerwin WS, Osman NF, Prince JL. Image processing and analysis in tagged cardiac MRI. In: Bankman I, editor. Handbook of medical image processing. New York: Academic Press; 1999.
13. Osman NF, Kerwin WS, McVeigh ER, Prince JL. Cardiac motion tracking using CINE harmonic phase (HARP) magnetic resonance imaging. Magn Reson Med 1999;42:1048–1060.
14. Garot J, Bluemke D, Osman NF, Rochitte C, McVeigh ER, Zerhouni EA, Prince JL, Lima J. Fast determination of regional myocardial strain fields from tagged cardiac images using harmonic phase (HARP) magnetic resonance imaging. Circulation 2000;101:981–988.
15. Osman NF, Prince JL. Visualizing myocardial function using HARP MRI. Phys Med Rio 2000;45:1665–1682.
16. Osman NF, McVeigh ER, Prince JL. Imaging heart motion using harmonic phase MRI. IEEE Trans Med Imag 2000;19:186–202.
17. Shinnar M, Leigh JS. Inversion of the Bloch equation. J Chem Phys 1993;98:6121–6128.
18. Osman NF, Sampath S, Prince JL, editors. Measuring 3D myocardial strain in a thin slice using harmonic phase MRI. In: Proc SPIE, 2000 Medical Imaging Conference.
19. Osman NF. Measuring regional cardiac function using harmonic phase magnetic resonance imaging. PhD thesis, Johns Hopkins University, 2000.
20. Atalar E, McVeigh ER. Minimization of dead-periods in MRI pulse sequences for imaging oblique planes. Magn Res Med 1994;32:773–777.
21. Young AA, Axel L. Three-dimensional motion and deformation of the heart wall: estimation with spatial modulation of magnetization—a model-based approach. Radiology 1992;185:241–247.
22. Arnini AA, Chen Y, Curwen RW, Mani V, Sun J. Coupled B-snake grids and constrained thin-plate splines for analysis of 2-D tissue deformations from tagged MRI. IEEE Trans Med Imag 1998;17:344–356.
23. O'Dell WG, Moore CC, Hunter WC, Zerhouni EA, McVeigh ER. Three-dimensional myocardial deformations: calculation with field fitting to tagged MR images. Radiology 1995;195:829–835.
24. Robson MD, Constable RT. Three-dimensional strain-rate imaging. Magn Reson Med 1996;36:537–546.
25. Axel L, Dougherty L. System and method for magnetic resonance imaging of 3-dimensional heart wall motion with spatial modulation of magnetization. U.S. Patent 5111820; 1990.